Substituent Effects Provide Access to Tetrasubstituted Ring-Opening Olefin Metathesis of Bicyclo[4.2.0]oct-6-enes

Gyusaang Youn and Nicole S. Sampson*

Cite This: *ACS Org. Inorg. Au* 2021, 1, 29–36

Read Online

ACCESS | Metrics & More | Article Recommendations | Supporting Information

ABSTRACT: Herein, we report the origin of unexpected reactivity of bicyclo[4.2.0]oct-6-ene substrates containing an α,β-unsaturated amide moiety in ruthenium-catalyzed alternating ring-opening metathesis polymerization reactions. Specifically, compared with control substrates bearing an ester, alkyl ketone, nitrile, or tertiary amide substituent, α,β-unsaturated substrates with a weakly acidic proton showed increased rates of ring-opening metathesis mediated by Grubbs-type ruthenium catalysts. ^{1}H NMR and IR spectral analyses indicated that deprotonation of the α,β-unsaturated amide substrates resulted in stronger coordination of the carbonyl group to the ruthenium metal center. Principal component analysis identified ring strain and the electron density on the carbonyl oxygen (based on structures optimized by means of ωB97X-D/6311+G(2df,2p) calculations) as the two key contributors to fast ring-opening metathesis of the bicyclo[4.2.0]oct-6-enes; whereas the dipole moment, conjugation, and energy of the highest occupied molecular orbital had little to no effect on the reaction rate. We conclude that alternating ring-opening metathesis polymerization reactions of bicyclo[4.2.0]oct-6-enes with unstrained cycloalkenes require an ionizable proton for efficient generation of alternating polymers.

KEYWORDS: ring-opening olefin metathesis, ionizable protons, tetrasubstituted alkenes, carbonyl coordination, principal component analysis
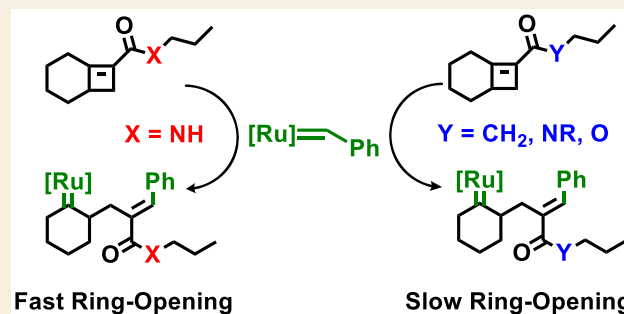
INTRODUCTION

Precise construction of polymer backbones and their side chains is crucial for state-of-the-art control of polymer microstructures. In living organisms, sequence-defined biomacromolecules such as proteins and DNA can be of central importance in the development, functioning, and reproduction in living organisms.[1] These perfectly monodispersed macromolecules with predetermined sequences are able to store information in which they translate into functional and structural properties.[2–5] Such molecules exhibit a one-to-one relationship between sequence and properties.[6] Therefore, the ability to construct a highly organized synthetic architecture would remarkably benefit applications in many fields including biomedicine and nanotechnology.[7]

Alternating copolymers are sequence-controlled polymers which feature a nonconsecutive sequence of the same monomeric unit in the same precise order.[8,9] Alternating copolymers can be prepared via a traditional radical polymerization,[10] or controlled radical polymerization such as reversible addition–fragmentation chain transfer (RAFT)[4] and atom transfer radical polymerization (ATRP).[11] Perfect alternation occurs when each of the propagating species prefers to add the other monomer rather than react with its own type of monomer. However, many alternating copolymerization systems do not strictly alternate due to some degree of

homoaddition being present.[12] Alternating ring-opening metathesis polymerization (AROMP) has enabled access to well-controlled architectures by the convenient installation of a precise number of carbon spacers between functional monomers.[13–16] Alternating copolymers prepared by AROMP present superior monomer economics and functionalities that are often required in multiple applications such as tunability and degradability.[17–19]

In previous work, we demonstrated the AROMP of a series of carboxymethyl bicyclo[n.2.0] monomers, including methyl bicyclo[4.2.0]oct-7-ene-7-carboxylate (M1), which can be used to generate perfectly alternating M1/cyclohexene polymers (Figure 1).[20] In addition, we extended the reaction to bicyclo[4.2.0]oct-7-ene amides (M1 amides), which, upon AROMP, isomerize to bicyclo[4.2.0]oct-6-ene amides (M2 amides).[13] This process provides tetrasubstituted alkene monomers, which are sterically less accessible than trisubstituted alkene monomers. Owing to their inaccessibility to
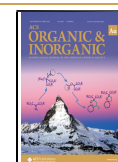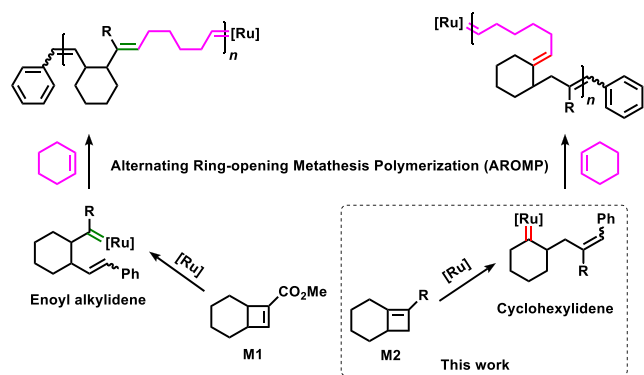
Figure 1. ROM as the initiation step in AROMP of bicyclo[4.2.0]-octene substrates.

metal catalysts, tetrasubstituted alkenes generally show little to no reactivity in olefin metathesis. To date, tetrasubstituted alkenes have been reported only as metathesis products and not as ring-opening substrates.[21] Despite the challenges posed by these alkenes, we successfully developed a method for AROMP of bicyclo[4.2.0]oct-6-enes bearing a few functional

groups.[22] Fast initiation and propagation are critical for obtaining polymers with controlled molecular weight and narrow molecular weight distribution. To better understand substrate reactivity and to develop a systematic approach for monomer selection, we conducted a series of mechanistic studies of the initiation step of AROMP, that is, ring-opening metathesis (ROM). Herein we report on our investigation of the unusual reactivity of tetrasubstituted bicyclo[4.2.0]oct-6-enes and demonstrate the importance of functional groups in the ROM step.

RESULTS AND DISCUSSION

First, we analyzed the kinetics and products of ruthenium-catalyzed ROM of bicyclo[4.2.0]oct-6-ene derivatives M2 by measuring the rate of substrate consumption (Table 1). Each M2 substrate was allowed to react with an equimolar amount of ruthenium carbene (designated [Ru]); then the reaction was quenched with ethyl vinyl ether, and the products were isolated and characterized. In all cases, quenching yielded products with an *exo*-methylene group on the cyclohexane ring (3), indicating regioselective formation of a ruthenium cyclohexylidene species ([Ru]=M2). During each reaction, the concentration of substrate was periodically monitored by

Table 1. Rates of ROM for Bicyclo[4.2.0]oct-6-ene Substrates Mediated by Ruthenium Carbene Species
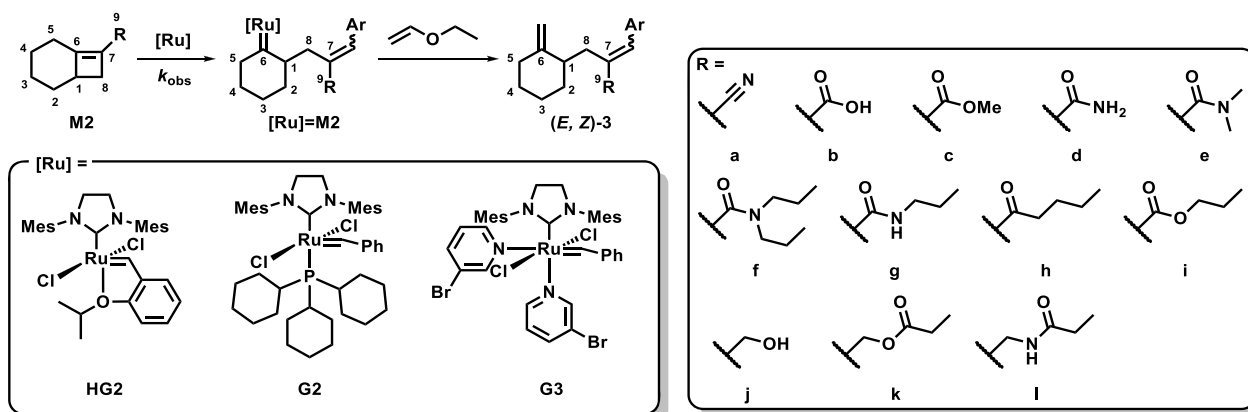
entry	[Ru][a]	substrate	k_{obs}[b]	$t_{1/2}$ (min)[c]	E/Z[d]	yield 3 (%)[d]
1	G3	M2a	1.54×10^{-5} s^{-1}	749.7	57:43	79
2	G3	M2b	1.34×10^{-4} s^{-1}	85.9	86:14	16
3	G3	M2c	1.50×10^{-4} M^{-1} s^{-1}	1227.4	78:22	n.d.
4	G3	M2d	1.85×10^{-2} M^{-1} s^{-1}	13.3	92:8	93
5	G3	M2e	3.04×10^{-6} M^{-1} s^{-1}	83289.4	n.d.	n.d.
6	G3	M2f	1.36×10^{-5} M^{-1} s^{-1}	15854.0	n.d.	n.d.
7	HG2	M2g	2.90×10^{-5} s^{-1}	398.9	74:26	88
8[e]	HG2	M2g	5.70×10^{-5} s^{-1}	202.7	n.d.	95
9	G2	M2g	2.44×10^{-3} M^{-1} s^{-1}	88.0	84:16	95
10[f]	G3	M2g	5.13×10^{-3} M^{-1} s^{-1}	41.9	94:6	91 (82[g])
11	G3	M2h	3.96×10^{-5} M^{-1} s^{-1}	5093.0	84:16	43
12[f]	G3	M2i	4.16×10^{-5} M^{-1} s^{-1}	5191.6	78:22	68
13	G3	M2j	5.13×10^{-4} s^{-1}	22.5	91:9	96
14	G3	M2k	6.46×10^{-4} s^{-1}	17.9	98:2	95
15	G3	M2l	8.44×10^{-4} s^{-1}	13.7	82:18	88

[a]The ruthenium carbene and the substrate were used in equimolar amounts (80 mM in CDCl$_3$), and the concentrations of all the substrates over time were measured by means of quantitative ^{1}H NMR spectroscopy using hexamethylcyclotrisiloxane as an internal standard. [b]Observed rate constants (k_{obs}) for each reaction were extracted from the corresponding integrated rate equation with the best nonlinear least-squares fit. [c]The first half-lives of each substrate were calculated from k_{obs} values. [d]Determined by ^{1}H NMR spectroscopy; n.d. = not determined. [e]The reaction was carried out with 1 equiv of *N*,*N*-diisopropylethylamine. [f]Because of the limited availability of the substrates and the ruthenium reagent, triplicate repeatability was assessed only on these substrates. [g]Isolated yield.

means of quantitative ^{1}H NMR spectroscopy with hexamethylcyclotrisiloxane as an internal standard. The time courses of the obtained substrate concentrations were fit to an integrated rate equation using nonlinear least-squares fitting (Supporting Information). The first half-life of each substrate was determined from its observed rate constant (k_{obs}), which was extracted from the best nonlinear least-squares fit.

The substrates (Table 1) could be grouped on the basis of their consumption rates during ROM. One group comprised substrates with an ionizable proton (entries 2, 4, 10, 13, and 15), which underwent considerably faster ROM than substrates without an ionizable proton (entries 1, 3, 5, 6, 11, and 12). For example, substrates with no amide protons were much less reactive than substrates with amide protons (compare M2d and M2g with M2e and M2f, respectively); and similar results were observed for acid M2b versus esters M2c and M2i. We perceived this as an ionizable proton rather than an acidic proton because we found no clear correlation between pK_a and the rate of ROM.

Another group was composed of substrates with an α,β-unsaturated moiety (entries 1−6 and 10−12); these substrates were consumed more slowly than the unconjugated substrates (entries 13−15) consistent with conjugation decreasing the electron density around the alkene, making it less reactive toward ruthenium. Natural bond orbital (NBO) calculations indicated that the $\pi_{C6−C7}$ energy for α,β-unsaturated substrate M2i was 7.56 kcal/mol lower than that of its unconjugated analogue M2k. Masking an ionizable proton decreased the rate of ROM for α,β-unsaturated substrates, whereas masking the proton of unconjugated substrate M2j by acylation of the hydroxy group to afford M2k slightly increased the rate of ROM (compare entries 13 and 14). Studies suggest that the decomposition of ruthenium alkylidene by alcohols could potentially contribute to the slower ROM in M2j than M2k.[23−26] However, we observed the same rates of consumption for substrate (M2j) and ruthenium alkylidene (G3) via ^{1}H NMR monitoring which indicates that decomposition of ruthenium alkylidene is absent. The increased ROM rate in M2k may be due to the slightly increased electron density around the alkene caused by acylation, which limits oxygen inductive effects on the electron density of the alkene. In contrast, the alcohol functionality in M2j can inductively draw electron density from the alkene resulting in decreased reactivity in ROM.

Substrate half-life increased as the steric bulk of the functional group increased, although the correlation between ROM rate and the increase in steric bulk was not linear (M2d < M2g < M2f and M2b < M2c < M2i). Notably, the low yield of 3b (entry 2) was due to a side reaction that yielded a lactone, (E)-3-benzylidene-3,4,4a,5,6,7-hexahydro-2H-chromen-2-one, as the major product (see the Supporting Information for the structure). The acidity of M2b may have triggered an O-insertion reaction of the ruthenium cyclohexylidene species and subsequent β-hydride elimination to yield the lactone and eventually caused ruthenium species degradation.[27]

Xia and co-workers reported that cyclopropene derivatives with significant steric bulk around the alkene can undergo AROMP with unstrained cyclic olefins such as cyclohexene.[28] Our group found that M2 substrates with carboxylic acid and ethyl ester functionalities can slowly undergo AROMP with cyclohexene, but conversion is very low. In contrast, M2 substrates with nitrile and propyl amide moiety underwent

successful AROMP, indicating that steric bulk is not the major contributor for AROMP.[22] During ROM of M2 substrates, chelation of oxygen to ruthenium has less influence on unconjugated systems than on conjugated systems; these results differ from those obtained with cyclopropene derivatives. It is worth noting that the lack of conjugation in a substrate makes its ROM reactivity more sensitive to the electron density of the alkene.

We propose that, depending on the functional group on the bicyclo[4.2.0]oct-6-ene substrates, the [2 + 2] cycloaddition reaction can proceed by one of the three transition states depicted in Figure 2. The reactions of unconjugated substrates
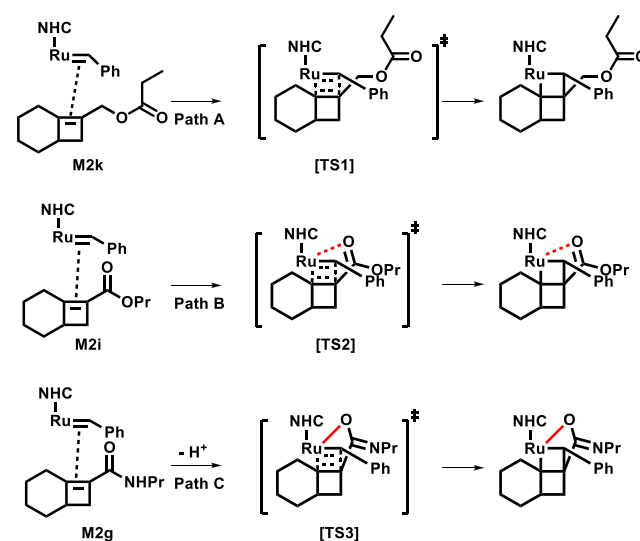

Figure 2. Proposed functional-group-dependent reaction paths and transition states. Paths A−C involve, respectively, a traditional [2 + 2] cycloaddition, a [2 + 2] cycloaddition with carbonyl coordination, and a [2 + 2] cycloaddition with carbonyl coordination enhanced by deprotonation. Chloride ligands have been omitted for clarity.

proceed via a traditional [2 + 2] cycloaddition process (Path A, TS1). In contrast, during reactions of substrates with α,β-unsaturated carbonyl moieties, the transition state involving the ruthenium alkylidene species can be stabilized by coordination of the carbonyl oxygen to the ruthenium metal center (Paths B and C, TS2 and TS3). Despite this stabilization of the transition state, ROM of α,β-unsaturated substrates is expected to be slower than ROM of unconjugated substrates because of the lower electron density around the alkene in the former (Path B). In contrast, ROM of α,β-unsaturated acid M2b and amides M2d and M2g, each of which has an ionizable proton, can be facilitated by deprotonation, which further stabilizes the transition state by the interaction of the nitrogen lone pair with the C−N antibonding orbital (Path C). We hypothesize that this deprotonation increases the rate of ROM. NBO calculations support the correlation between the ROM rate and the natural electron population of the carbonyl oxygen of deprotonated species (see the Supporting Information for natural electron population values). The enhanced coordination between the carbonyl group and the ruthenium compensates for the conjugation-induced decrease in the electron density of the alkene. Therefore, the rates of ROM of α,β-unsaturated substrates with an ionizable proton (M2b, M2d, and M2g) were much faster than the rates for substrates without an
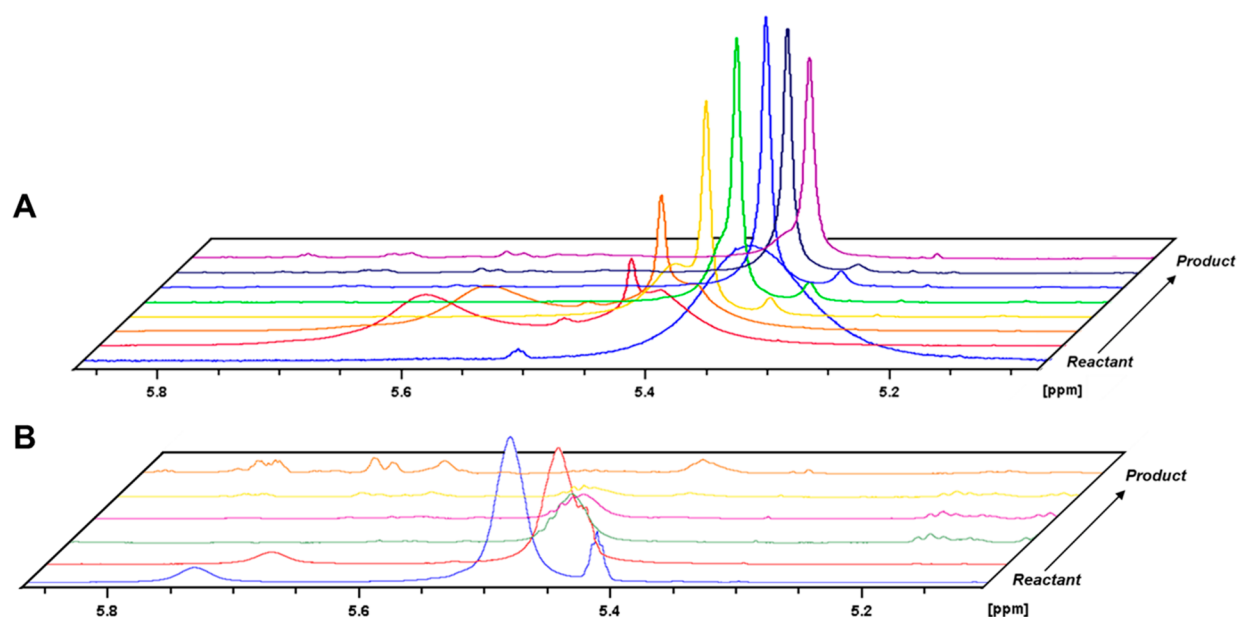
Figure 3. ^{1}H NMR spectral analysis of ROM reactions of M2d (A) and M2g (B) as a function of time, showing the disappearance of the amide protons over time.
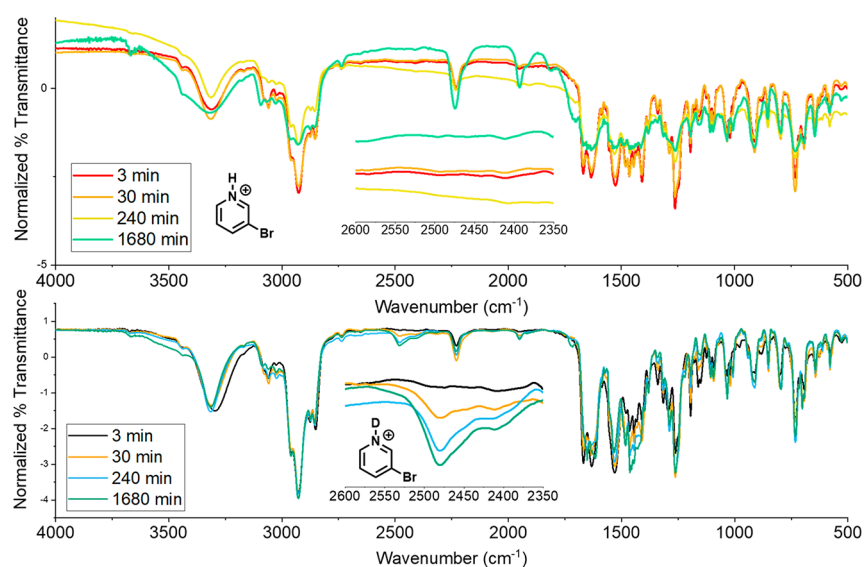

Figure 4. Fourier transform IR spectral analysis of ROM reactions of M2g (top) and deuterated M2g-D (bottom) with G3 as a function of time. The peak at 2480 cm^{-1} corresponds to the N−D stretching vibration of the deuterated 3-bromopyridine ligand of G3.

ionizable proton, and the former substrates were almost as reactive as the unconjugated substrates (M2j, M2k, and M2l).

To test our hypothesis, we evaluated a ruthenium species bearing a nonbasic ligand, o-isopropoxybenzylidene (HG2), in the ROM of M2g. We expected that ROM with this ligand would be slower than ROM with G2 or G3 if removal of an ionizable proton does in fact affect the rate of ROM. Indeed, we found that the half-life of M2g in a reaction with HG2 was 9.5 times higher than in a reaction with G3 (compare entries 7 and 10 in Table 1). Although the slower rates of conversion may have been partially due to the slower dissociation of the o-isopropoxybenzylidene ligand in HG2 compared to the tricyclohexylphosphine in G2 or the 3-bromopyridine in G3, adding 1 equiv of N,N-diisopropylethylamine as an external base with HG2 increased the rate of ROM by a factor of 2 (compare entries 7 and 8). These results clearly confirmed that

the deprotonated substrates underwent faster ROM. Finally, the rate of ROM in the presence of ligand G2 (entry 9), which contains a basic tricyclohexylphosphine moiety, was slightly slower than the rate with G3 ($k_{G2/M2g}/k_{G3/M2g} = 0.48$); but the decrease was not as marked as that observed with HG2.

To determine how deprotonation induced carbonyl coordination to ruthenium, as well as how other factors associated with the substrates contributed to faster ROM, we monitored the ^{1}H NMR signals of the amide protons of M2d and M2g during ROM. Figure 3 shows the amide regions for M2d and M2g in ^{1}H NMR spectra measured during G3-mediated ROM as a function of time. In both cases, the amide proton disappeared over the course of the reaction and then reappeared after the reaction was quenched with ethyl vinyl ether, indicating that dissociation of the product from the ruthenium restored the ionizable proton. Upon addition of G3
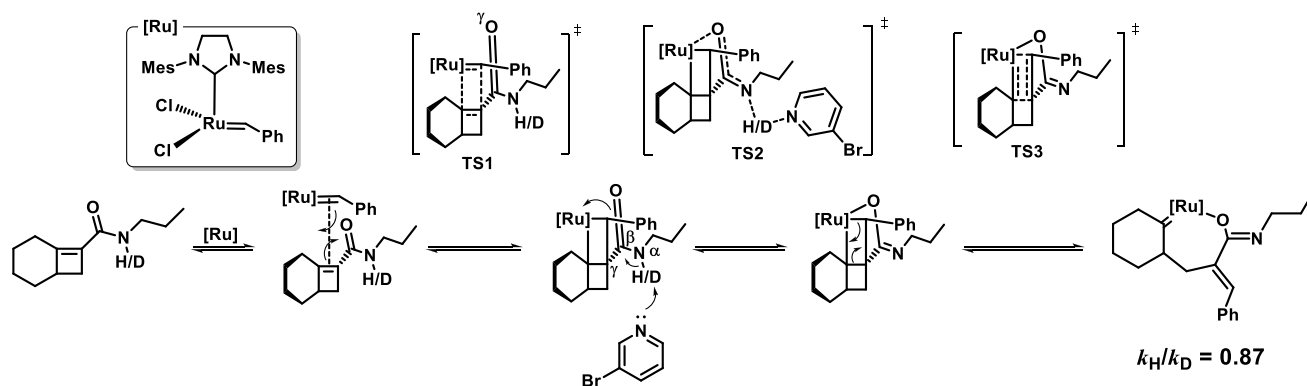
Figure 5. KIE on ROM of M2g and suggested [Ru]−O bond formation during ROM.

to M2d, the peak for the two indistinguishable NH protons of M2d split into two peaks. One peak eventually disappeared while the other became sharper. This behavior can be viewed as indicating the formation of an imidic acid type ruthenium adduct (Figure 2, Path C).

In addition, we observed the generation of a deuterated pyridinium species by means of Fourier transform IR spectral analysis of the ROM reaction of M2g-D with G3 as a function of time (Figure 4). The peak at 2480 cm^{-1} corresponds to the deuterated 3-bromopyridine formed by transfer of deuterium from M2g-D. Furthermore, the absence of a peak at 2480 cm^{-1} and the broadening of the N−H stretch band at 3325 cm^{-1} observed in the spectra for ROM of M2g indicate the removal of the amide proton by 3-bromopyridine.

To probe the magnitude of the stabilization of the transition state by interaction between the carbonyl oxygen and the ruthenium center in the transition state of Path C in Figure 2, we measured the kinetic isotope effect (KIE, k_H/k_D; Figure 3). The ionizable proton of M2g was labeled with deuterium, and then the rate of ROM of M2g-D was compared with that of M2g-H by means of ^{1}H NMR spectroscopy. We observed an inverse KIE value (0.87). Guironnet and co-workers proposed a free energy profile for the initiation of G3 with norbornene in ROMP.[29] They suggest that carbonyl coordination can cause slow ROM. However, we observe fast ROM in M2k, a substrate with an ionizable proton. The two 3-bromopyridines on G3 are expected to dissociate to form the 14-electron active carbene species. The presence of the weak pyridine base may facilitate deprotonation of the ionizable amide whose pK_a will shift upon carbonyl coordination to the ruthenium carbene. Alteration of this equilibrium upon isotopic substitution of the amide NH leads to an apparently inverse equilibrium isotope effect (EIE), which precedes the rate-determining step and is observed as an inverse KIE for the overall ROM process.[30−32] An equilibrium deprotonation step prior to the formation of the product suggests that the stabilization of transition state (TS2) occurs when Ru−O is generated from the deprotonated amide (Figure 5). The generation of Ru−O bond does not involve displacement of a chloride and the oxygen lone pair is donated to the ruthenium center to generate a 16-electron ruthenium carbene. More research is needed to confirm whether the deprotonation is concerted or stepwise.

Next, we performed NBO calculations to further strengthen our hypothesis of the Ru−O bond formation after deprotonation. The geometries and vibrational frequencies of each substrate were first optimized by means of Gaussian calculations using the ωB97X-D functional and the 6-

311+G(2df,2p) basis set.[33] Natural population analysis confirmed that the electron density on the carbonyl oxygen increased upon removal of an ionizable proton (Supporting Information). This increased electron density is expected to result in stronger coordination of the carbonyl oxygen to the ruthenium center in the deprotonated species than in the protonated species.

Although we have shown that the presence of ionizable proton in α,β-unsaturated substrates undergo fast ROM, the presence of an ionizable proton is insufficient to provide a comprehensive understanding of the ROM reactivity of M2 substrates. To gain additional insight into the weighting by which other factors contribute to the rate of ROM, we performed principal component analysis (PCA, Supporting Information). The range of ROM half-lives for the M2 substrates is shown in Figure 6A. The values of C=C
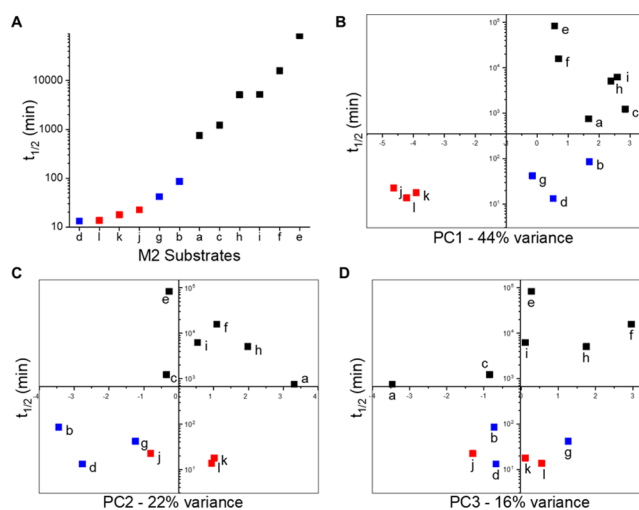

Figure 6. Plot of the first half-lives of M2 substrates (time for consumption of first 50% of M2) (A) and plots of the first half-lives of M2 substrates against each PC (B−D). Unconjugated substrates (red), α,β-unsaturated substrates with an ionizable proton (blue), and α,β-unsaturated substrates without ionizable protons (black).

stretching vibrations, the electron densities and partial charges at the alkene and adjacent carbons, and the dipoles and the energies of the highest occupied and lowest unoccupied molecular orbitals of the M2 substrates were calculated and imported from the NBO calculations. The calculations were based on the deprotonated structure for the α,β-unsaturated

substrates containing ionizable protons (M2b, M2d, and M2g). In addition, we assessed the sterics of each substrate by computing the cavity surface areas and volumes by means of the GEPOL (GEnerating POLyhedra) algorithm using the SMD solvation model with water as a solvent.[34−36] Each variable was standardized prior to PCA. Detailed information for principal component analysis, including eigenvalues and a scree plot, is available in the Supporting Information. We successfully used PCA to classify the substrates into three principal components. We were able to explain 82% of the data set by adopting three principal components (PCs). As indicated by the percentage of variance for each PC, PC1 had the most significant weighting factor (44%), followed by PC2 (22%) and PC3 (16%). We chose a coefficient value of 0.3 for each variable in the individual PC as a significant cutoff value. The half-lives of each substrate are dependent variables that should not be included in the PCA because of the risk of heteroscedasticity. Therefore, separate plots were generated to visualize the correlation between each principal component and the half-lives of substrate (Figure 6B−D).

PC1 strongly correlates with the electron densities on C6, C7, and C9, the vibrational frequency of C6=C7, the energy of the lowest unoccupied molecular orbital, and the presence of conjugation. In Figure 6B, the substrates cluster into three groups based on half-lives and PC1: unconjugated (red), conjugated with ionizable proton (blue), conjugated without ionizable proton (black). Variables that are strongly correlated with PC1 influence the rate of ROM.

PC2 strongly correlates with the electron density on the carbonyl oxygen, the partial charges at C7, C9, and the carbonyl oxygen, and the presence of an ionizable proton. In Figure 6C, the α,β-unsaturated substrates containing an ionizable proton (blue) are clearly distinguished from the α,β-unsaturated substrates without an ionizable proton (black). The relationship between half-life and principal components of substrates shown above is in line with the observations from ^{1}H NMR and Fourier transform IR spectral analyses (Figures 3 and 5).

PC3 strongly correlates with the cavity surface area and cavity volume of the substrates. The relationship between steric bulk and the rate of ROM was assessed by plotting PC3 against the half-lives of M2 (Figure 6D). Although the steric bulk of the M2 substrates explains the rate trend for substrates with the same functionalities to some extent (M2d < M2g < M2f and M2b < M2c < M2i), the rate trend between different functionalities is not clearly distinguished. Also, the effect of steric bulk in unconjugated substrates is marginal (M2j, M2k, and M2l), meaning that sterics play only a minor role in the ROM reactions of the M2 substrates. A plot of PC1−PC2 projection against the inverse of ROM half-lives (Figure 7) demonstrates that substrates with higher vibrational frequencies (indicating loss of conjugation and larger ring strain) are separately grouped (M2i, M2j, and M2k) and show higher ROM rates. Substrates with an ionizable proton (M2b, M2d, and M2g) are segregated from the other α,β-unsaturated substrates (M2c, M2e, M2f, M2h, and M2i). These results clearly show the dependence of the ROM rate on the electron density of the carbonyl oxygen of these α,β-unsaturated substrates with an ionizable proton and are in good agreement with the observed ROM rates, whereas sterics (PC3) do not predict ROM reactivity (Figures 6D and S63).
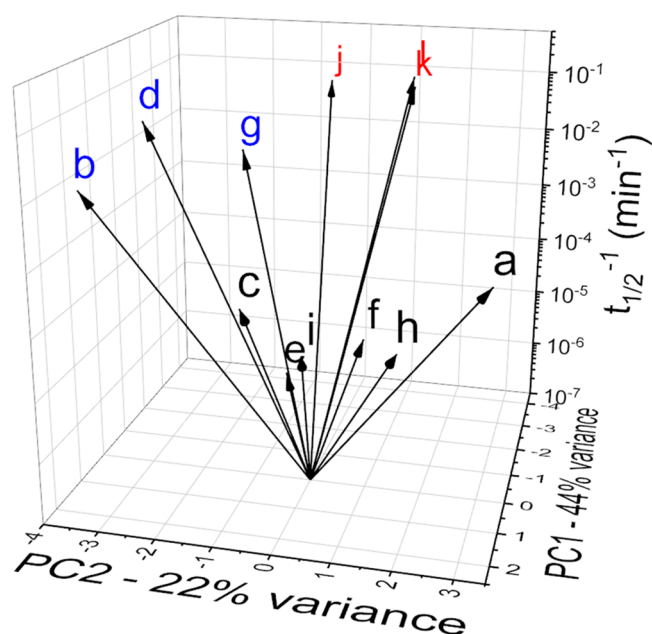

Figure 7. Three-dimensional plot of PC1, PC2, and the inverse of the first half-lives of M2 substrates (time for consumption of first 50% of M2) during ROM. Unconjugated substrates (red), α,β-unsaturated substrates with an ionizable proton (blue), and α,β-unsaturated substrates without ionizable protons (black).

CONCLUSION

We investigated how functional groups affect ROM reactions of bicyclo[4.2.0]oct-6-enes M2, specifically how deprotonation of an ionizable proton overcomes the steric barrier to tetrasubstituted alkene metathesis. We identified the key contributing factors to the ROM rate for these compounds. PCA demonstrated that the key factors affecting the rate are the ring strain (as indicated by the vibrational frequency of C6=C7) and the electron density around the carbonyl oxygen. The latter was increased by the removal of an ionizable proton, which resulted in stronger coordination of the carbonyl oxygen to the ruthenium metal center. The stronger coordination stabilized the ROM transition state and thus allowed for faster ring-opening. The effect of the stronger coordination overcame the attenuation of the ROM rate due to the decreased electron density around the alkene in α,β-unsaturated substrates. The accelerated overall rate of ROM reactions of AROMP monomers can be expected to result in polymers with higher molecular weights and narrower dispersities. Therefore, we anticipate that our findings will guide the selection of appropriate monomers for effective AROMP.

ASSOCIATED CONTENT

Ⓢ Supporting Information

The Supporting Information is available free of charge at https://pubs.acs.org/doi/10.1021/acsorginorgau.1c00016.

> Synthesis and characterization of all newly prepared compounds, computational methods, ROM kinetic data, and details regarding the PCA (PDF)

■ AUTHOR INFORMATION

Corresponding Author

Nicole S. Sampson − *Department of Chemistry, Stony Brook University, New York 11790-3400, United States;*
  orcid.org/0000-0002-2835-7760;
  Email: Nicole.sampson@stonybrook.edu

Author

Gyusaang Youn − *Department of Chemistry, Stony Brook University, New York 11790-3400, United States;*
  orcid.org/0000-0002-9152-1367

Complete contact information is available at:
https://pubs.acs.org/10.1021/acsorginorgau.1c00016

Author Contributions

The manuscript was written through contributions of all authors. All authors have given approval to the final version of the manuscript.

Notes

The authors declare no competing financial interest.

■ ABBREVIATIONS

AROMP, alternating ring-opening metathesis polymerization; KIE, kinetic isotope effect; NBO, natural bond orbital; PC, principal component; PCA, principal component analysis; RDS, rate-determining step; ROM, ring-opening metathesis

■ REFERENCES

(1) Lutz, J. F.; Ouchi, M.; Liu, D. R.; Sawamoto, M. Sequence-controlled polymers. *Science* **2013**, *341* (6146), 1238149.
(2) Schnitzler, T.; Herrmann, A. DNA block copolymers: Functional materials for nanoscience and biomedicine. *Acc. Chem. Res.* **2012**, *45* (9), 1419−30.
(3) Huang, J.; Bonduelle, C.; Thevenot, J.; Lecommandoux, S.; Heise, A. Biologically active polymersomes from amphiphilic glycopeptides. *J. Am. Chem. Soc.* **2012**, *134* (1), 119−22.
(4) Huang, Z.; Noble, B. B.; Corrigan, N.; Chu, Y.; Satoh, K.; Thomas, D. S.; Hawker, C. J.; Moad, G.; Kamigaito, M.; Coote, M. L.; Boyer, C.; Xu, J. Discrete and stereospecific oligomers prepared by sequential and alternating single unit monomer insertion. *J. Am. Chem. Soc.* **2018**, *140* (41), 13392−13406.
(5) Song, Z.; Fu, H.; Wang, J.; Hui, J.; Xue, T.; Pacheco, L. A.; Yan, H.; Baumgartner, R.; Wang, Z.; Xia, Y.; Wang, X.; Yin, L.; Chen, C.; Rodriguez-Lopez, J.; Ferguson, A. L.; Lin, Y.; Cheng, J. Synthesis of polypeptides via bioinspired polymerization of in situ purified n-carboxyanhydrides. *Proc. Natl. Acad. Sci. U. S. A.* **2019**, *116* (22), 10658−10663.
(6) Crick, F. Central dogma of molecular biology. *Nature* **1970**, *227* (5258), 561−3.
(7) Engelis, N. G.; Anastasaki, A.; Nurumbetov, G.; Truong, N. P.; Nikolaou, V.; Shegiwal, A.; Whittaker, M. R.; Davis, T. P.; Haddleton, D. M. Sequence-controlled methacrylic multiblock copolymers via

(8) Lutz, J.-F. Sequence-controlled polymerizations: The next holy grail in polymer science? *Polym. Chem.* **2010**, *1* (1), 55−62.
(9) Nishimori, K.; Ouchi, M. Ab-alternating copolymers via chain-growth polymerization: Synthesis, characterization, self-assembly, and functions. *Chem. Commun. (Cambridge, U. K.)* **2020**, *56* (24), 3473−3483.
(10) Alfrey, T.; Lavin, E. The copolymerization of styrene and maleic anhydride. *J. Am. Chem. Soc.* **1945**, *67* (11), 2044−2045.
(11) Chen, G.-Q.; Wu, Z.-Q.; Wu, J.-R.; Li, Z.-C.; Li, F.-M. Synthesis of alternating copolymers of N-substituted maleimides with styrene via atom transfer radical polymerization. *Macromolecules* **2000**, *33* (2), 232−234.
(12) Huang, J.; Turner, S. R. Recent advances in alternating copolymers: The synthesis, modification, and applications of precision polymers. *Polymer* **2017**, *116*, 572−586.
(13) Tan, L.; Li, G.; Parker, K. A.; Sampson, N. S. Ru-catalyzed isomerization provides access to alternating copolymers via ring-opening metathesis polymerization. *Macromolecules* **2015**, *48* (14), 4793−4800.
(14) Sui, X.; Zhang, T.; Pabarue, A. B.; Fu, L.; Gutekunst, W. R. Alternating cascade metathesis polymerization of enynes and cyclic enol ethers with active ruthenium fischer carbenes. *J. Am. Chem. Soc.* **2020**, *142* (30), 12942−12947.
(15) Pal, S.; Alizadeh, M.; Kilbinger, A. F. M. Telechelics based on catalytic alternating ring-opening metathesis polymerization. *ACS Macro Lett.* **2019**, *8* (10), 1396−1401.
(16) Elling, B. R.; Xia, Y. Living alternating ring-opening metathesis polymerization based on single monomer additions. *J. Am. Chem. Soc.* **2015**, *137* (31), 9922−6.
(17) Zhang, J.; Li, G.; Sampson, N. S. Incorporation of large cycloalkene rings into alternating copolymers allows control of glass transition and hydrophobicity. *ACS Macro Lett.* **2018**, *7* (9), 1068−1072.
(18) Boadi, F. O.; Zhang, J.; Yu, X.; Bhatia, S.; Sampson, N. S. Alternating ring-opening metathesis polymerization provides easy access to functional and fully degradable polymers. *Macromolecules* **2020**, *53* (14), 5857−5868.
(19) Elling, B. R.; Su, J. K.; Xia, Y. Degradable polyacetals/ketals from alternating ring-opening metathesis polymerization. *ACS Macro Lett.* **2020**, *9* (2), 180−184.
(20) Tan, L.; Parker, K. A.; Sampson, N. S. A bicyclo[4.2.0]octene-derived monomer provides completely linear alternating copolymers via alternating ring-opening metathesis polymerization (AROMP). *Macromolecules* **2014**, *47* (19), 6572−6579.
(21) Mukherjee, N.; Planer, S.; Grela, K. Formation of tetrasubstituted C−C double bonds via olefin metathesis: Challenges, catalysts, and applications in natural product synthesis. *Org. Chem. Front.* **2018**, *5* (3), 494−516.
(22) Chen, L.; Li, L.; Sampson, N. S. Access to bicyclo[4.2.0]octene monomers to explore the scope of alternating ring-opening metathesis polymerization. *J. Org. Chem.* **2018**, *83* (5), 2892−2897.
(23) Rowley, C. N.; van der Eide, E. F.; Piers, W. E.; Woo, T. K. DFT study of the isomerization and spectroscopic/structural properties of ruthenacyclobutane intermediates relevant to olefin metathesis. *Organometallics* **2008**, *27* (23), 6043−6045.
(24) Dinger, M. B.; Mol, J. C. Degradation of the second-generation grubbs metathesis catalyst with primary alcohols and oxygen − isomerization and hydrogenation activities of monocarbonyl complexes. *Eur. J. Inorg. Chem.* **2003**, *2003* (15), 2827−2833.
(25) Beach, N. J.; Lummiss, J. A. M.; Bates, J. M.; Fogg, D. E. Reactions of Grubbs catalysts with excess methoxide: Formation of novel methoxyhydride complexes. *Organometallics* **2012**, *31* (6), 2349−2356.
(26) Banti, D.; Mol, J. C. Degradation of the ruthenium-based metathesis catalyst [RuCl2(CHPh)(H2iPr)(PCy3)] with primary alcohols. *J. Organomet. Chem.* **2004**, *689* (20), 3113−3116.

(27) Bailey, G. A.; Foscato, M.; Higman, C. S.; Day, C. S.; Jensen, V. R.; Fogg, D. E. Bimolecular coupling as a vector for decomposition of fast-initiating olefin metathesis catalysts. *J. Am. Chem. Soc.* **2018**, *140* (22), 6931−6944.

(28) Elling, B. R.; Su, J. K.; Xia, Y. Polymerization of cyclopropenes: Taming the strain for the synthesis of controlled and sequence-regulated polymers. *Acc. Chem. Res.* **2021**, *54* (2), 356−365.

(29) Hyatt, M. G.; Walsh, D. J.; Lord, R. L.; Andino Martinez, J. G.; Guironnet, D. Mechanistic and kinetic studies of the ring opening metathesis polymerization of norbornenyl monomers by a grubbs third generation catalyst. *J. Am. Chem. Soc.* **2019**, *141* (44), 17918−17925.

(30) Baldwin, J. E.; Andrist, A. H. Mechanism and inverse primary kinetic isotope effect in the reaction of fluorenylidene with 3-deuteriocyclohexene. *J. Chem. Soc. D* **1971**, *23*, 1512−1513.

(31) Churchill, D. G.; Janak, K. E.; Wittenberg, J. S.; Parkin, G. Normal and inverse primary kinetic deuterium isotope effects for c-h bond reductive elimination and oxidative addition reactions of molybdenocene and tungstenocene complexes: Evidence for benzene sigma-complex intermediates. *J. Am. Chem. Soc.* **2003**, *125* (5), 1403−20.

(32) Gomez-Gallego, M.; Sierra, M. A. Kinetic isotope effects in the study of organometallic reaction mechanisms. *Chem. Rev.* **2011**, *111* (8), 4857−963.

(33) Frisch, M. J.; Trucks, G. W.; Schlegel, H. B.; Scuseria, G. E.; Robb, M. A.; Cheeseman, J. R.; Scalmani, G.; Barone, V.; Petersson, G. A.; Nakatsuji, H.; Li, X.; Caricato, M.; Marenich, A. V.; Bloino, J.; Janesko, B. G.; Gomperts, R.; Mennucci, B.; Hratchian, H. P.; Ortiz, J. V.; Izmaylov, A. F.; Sonnenberg, J. L.; Williams; Ding, F.; Lipparini, F.; Egidi, F.; Goings, J.; Peng, B.; Petrone, A.; Henderson, T.; Ranasinghe, D.; Zakrzewski, V. G.; Gao, J.; Rega, N.; Zheng, G.; Liang, W.; Hada, M.; Ehara, M.; Toyota, K.; Fukuda, R.; Hasegawa, J.; Ishida, M.; Nakajima, T.; Honda, Y.; Kitao, O.; Nakai, H.; Vreven, T.; Throssell, K.; Montgomery, J. A., Jr.; Peralta, J. E.; Ogliaro, F.; Bearpark, M. J.; Heyd, J. J.; Brothers, E. N.; Kudin, K. N.; Staroverov, V. N.; Keith, T. A.; Kobayashi, R.; Normand, J.; Raghavachari, K.; Rendell, A. P.; Burant, J. C.; Iyengar, S. S.; Tomasi, J.; Cossi, M.; Millam, J. M.; Klene, M.; Adamo, C.; Cammi, R.; Ochterski, J. W.; Martin, R. L.; Morokuma, K.; Farkas, O.; Foresman, J. B.; Fox, D. J. *Gaussian 16*, rev. C.01; Gaussian, Inc.: Wallingford, CT, 2016.

(34) Pascual-ahuir, J. L.; Silla, E.; Tuñon, I. Gepol: An improved description of molecular surfaces. III. A new algorithm for the computation of a solvent-excluding surface. *J. Comput. Chem.* **1994**, *15* (10), 1127−1138.

(35) Silla, E.; Tuñón, I.; Pascual-Ahuir, J. L. Gepol: An improved description of molecular surfaces. II. Computing the molecular area and volume. *J. Comput. Chem.* **1991**, *12* (9), 1077−1088.

(36) Pascual-Ahuir, J. L.; Silla, E. Gepol: An improved description of molecular surfaces. I. Building the spherical surface set. *J. Comput. Chem.* **1990**, *11* (9), 1047−1060.